Experimental Section

Synthesis of amorphous NiB_2

All chemicals were used as received without further purification. Amorphous NiB_2 was prepared by a reflux method with Ar protection[1]. Typically, 2.6 g $Ni_2SO_4·6H_2O$ was dissolved in 20 mL deionized water in three-necked flask. Then, 0.75 g $NaBH_4$ dissolved in 5 mL deionized water was rapidly added into the reaction flask. After refluxing for 2 h, the precipitates were collected and washed with deionized water/ethanol and then dried under vacuum.

Electrochemical measurements

Electrochemical measurements were carried out with an electrochemical workstation (CHI-760E Instruments, Shanghai Chenhua Instrument Corp., China). A conventional three-electrode cell was employed with a carbon cloth (CC) sample as working electrode, an Ag/AgCl electrode as reference electrode, and a graphite rod as counter electrode. Before coating catalyst on CC, the CC substrate was pretreated by soaking it in 0.5 M H_2SO_4 for 12 h, and then washed with deionized water several times and dried at 60 °C for 24 h. All potentials were referenced to reversible hydrogen electrode (RHE) by following equation: E_{RHE} (V)=$E_{Ag/AgCl}$+0.197+0.059×pH. The NORR tests were performed using an gastight H-type two-compartment electrochemical cell separated by a Nafion 211 membrane. Before the NORR measurements, all the feeding gases were purified through two glass bubblers containing 4 M KOH solution and the cathodic compartment was purged with Ar for at least 30 min to remove residual oxygen[2]. During each NORR electrolysis, high-purity NO gas (99.9%) was continuously purged into the cathodic chamber at a flow rate of 20 mL min^{-1}. After NORR electrolysis at specified potentials for 1 h, the aqueous and gas product are detected by the colorimetric methods and gas chromatography (GC), respectively.

Determination of NH_3

The generated NH_3 was determined by the indophenol blue method[3]. Typically, 0.5 mL of electrolyte was removed from the electrochemical reaction vessel and

diluted 10 times with deionized water. Then 2 mL of diluted solution was removed into a clean vessel followed by sequentially adding NaOH solution (2 mL, 1 M) containing salicylic acid ($C_7H_6O_3$, 5 wt.%) and sodium citrate ($C_6H_5Na_3O_7$, 5 wt.%), sodium hypochlorite (NaClO, 1 mL, 0.05 M), and sodium nitroprusside ($C_5FeN_6Na_2O$, 0.2 mL, 1wt.%) aqueous solution. After the incubation for 2 h at room temperature, the mixed solution was subjected to UV-vis measurement using the absorbance at 655 nm wavelength. The concentration-absorbance curves were calibrated by the standard NH_4Cl solution with a series of concentrations.

The detailed procedure for colorimetric determination of N_2H_4 was provided in our previous publications[4].

Calculations of NH_3 yield rate and NH_3-Faradaic efficiency

$$\mathrm{NH_3\ yield\ rate}\ (\mu \mathrm{g\ h^{-1}\ cm^{-2}}) = \frac{c_{\mathrm{NH_3}} \times V}{t \times A} \tag{1}$$

$$\mathrm{NH_3\text{-}Faradaic\ efficiency}\ (\%) = \frac{5 \times F \times c_{\mathrm{NH_3}} \times V}{17 \times Q} \times 100\% \tag{2}$$

where c_{NH3} (μg mL^{-1}) is the measured NH_3 concentration, V (mL) is the volume of the electrolyte, t (h) is the reduction time, A (cm^{-2}) is the surface area of CC (1×1 cm^2) , F (96500 C mol^{-1}) is the Faraday constant, Q (C) is the quantity of applied electricity.

Characterizations

X-ray diffraction (XRD) pattern was carried out on a Rigaku D/max 2400 diffractometer. Transmission electron microscopy (TEM), high-resolution transmission electron microscopy (HRTEM), selected area electron diffraction (SAED) and high-angle annular dark-field scanning transmission electron microscopy (HAADF-STEM) were recorded on a Tecnai G^2 F20 microscope. X-ray photoelectron spectroscopy (XPS) analysis was recorded on a PHI 5702 spectrometer. Online differential electrochemical mass spectrometry (DEMS, QAS 100) was performed by QAS 100 spectrometer.

Calculation details

The Cambridge sequential total energy package (CASTEP) module of the Materials Studio software was conducted for the quantum chemistry calculations. The

Perdew-Burke-Ernzerhof (PBE) generalized gradient approximation (GGA) functional was used for the exchange-correlation potential. The van der Waals interaction was described by using the empirical correction in Grimme's scheme (DFT+D). The convergence criteria for structure optimization were (1) energy tolerance of 1×10^{-5} eV, (2) maximum force tolerance of 0.02 eV $Å^{-1}$, (3) Monkhorst-Pack k-point sampling: 3 × 3 × 1. The electron wave functions were expanded using plane waves with a cutoff energy of 400 eV. NiB_2 (001) was modeled by a 3 × 3 supercell, and a vacuum region of 15 Å was used to separate adjacent slabs. The amorphous NiB_2 was built by relaxing the crystalline NiB_2 (001) at 600 K, and the atomic arrangement could be disordered.

The free energies (ΔG, 298 K) for each reaction were given after correction[5]:

$$\Delta G = \Delta E + \Delta ZPE - T\Delta S \tag{3}$$

where ΔE is the adsorption energy, ΔZPE is the zero-point energy difference and TΔS is the entropy difference between the gas phase and adsorbed state.

The Forcite module was employed for the MD simulations. The electrolyte system was modeled by a cubic cell with placing catalyst at the center of the cell and randomly filling 1000 H_2O, 50 NO molecules, and 50 H atoms. After geometry optimization, the MD simulations were performed under the universal field with the total simulation time of 5 ns at a time step of 1 fs.

The radial distribution function (RDF) is calculated by[6]

$$g(r) = \frac{dN}{4\pi\rho r^2 dr} \tag{4}$$

where d*N* is the amount of NO in the shell between the central particle r and r+dr, ρ is the number density of NO, H_2O, and H.

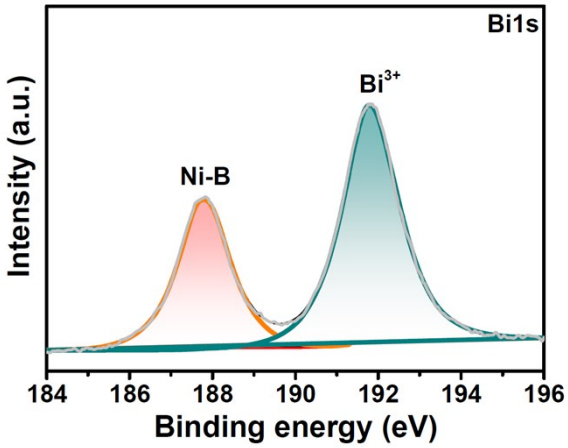

Fig. S1. XPS B1s spectra of NiB_2.

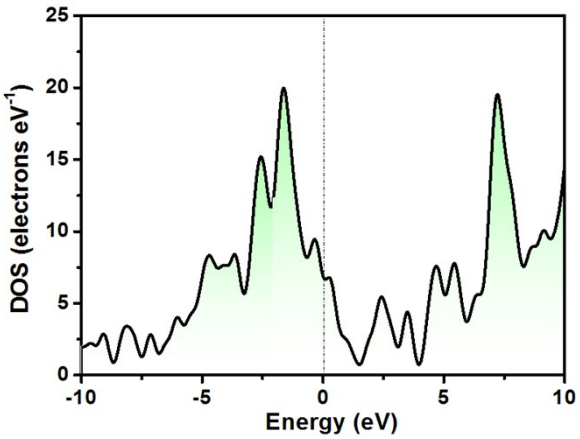

Fig. S2. DOS profile of NiB_2.

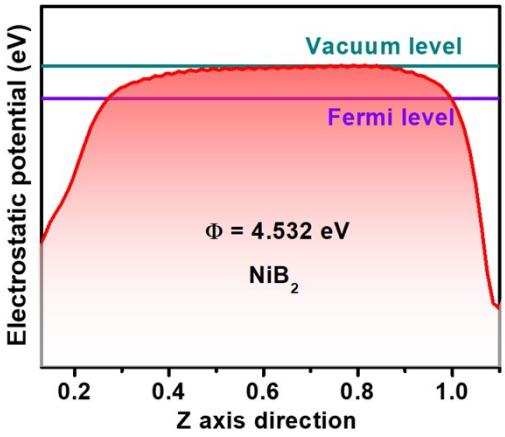

Fig. S3. Average potential profiles along c-axis direction for calculating the work function of NiB_2.

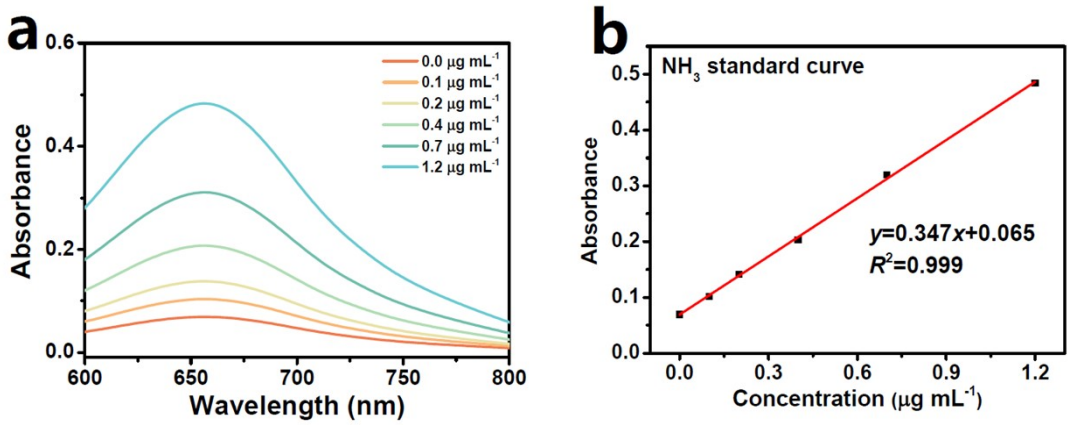

Fig. S4. (a) UV-vis absorption spectra of NH_4^+ assays after incubated for 2 h at ambient conditions. (b) Calibration curve used for the calculation of NH_3 concentrations.

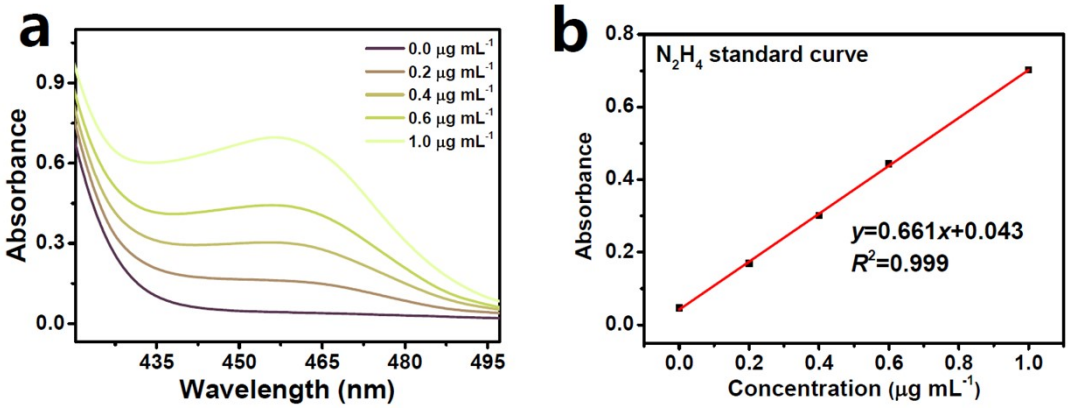

Fig. S5. (a) UV-vis absorption spectra of N_2H_4 assays after incubated for 20 min at ambient conditions. (b) Calibration curve used for calculation of N_2H_4 concentrations.

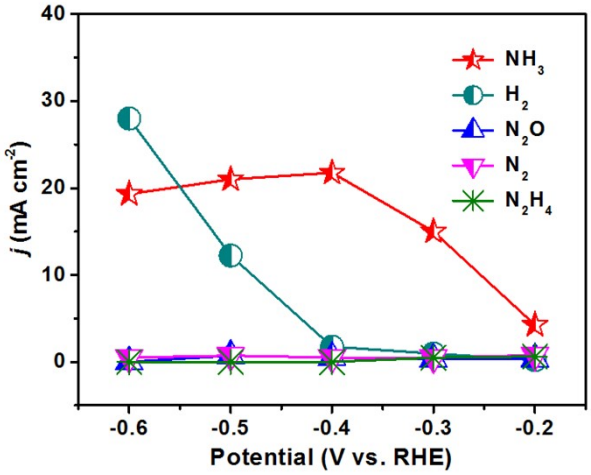

Fig. S6. Partial current densities of various products over NiB_2 after 1 h of NORR electrolysis at different potentials.

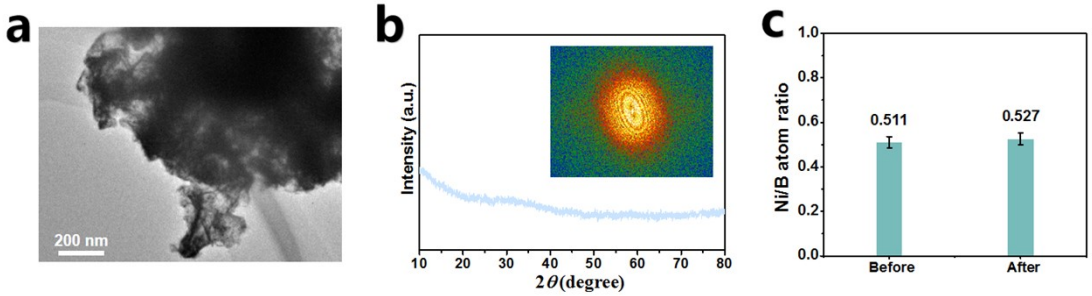

Fig. S7. (a) TEM image, (b) XRD pattern (inset: FFT pattern) and (c) Ni/B atom ratio of NiB_2 after stability tests.

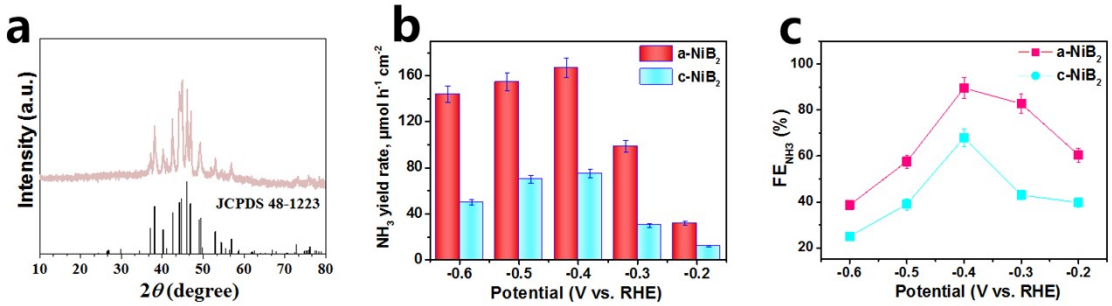

Fig. S8. (a) XRD pattern of crystalline NiB_2 (c-NiB_2). (b) NH_3 yield rates and (c) FE_{NH3} of c-NiB_2 and a-NiB_2.

The crystalline NiB_2 (c-NiB_2) is prepared by directly annealing amorphous NiB_2 (a-NiB_2) in Ar. The XRD pattern (Fig. S8a) shows the clear crystalline structure of c-NiB_2. Impressively, the NORR performance of c-NiB_2 is much inferior to that of a-NiB_2 in terms of both NH_3 yield rate (Fig. S8b) and FE_{NH3} (Fig. S8c), and the main cause for their performance disparity arises from their difference in electrochemical surface areas (ECSA), where a-NiB_2 exhibits a much higher ECSA than c-NiB_2 (Fig. S9).

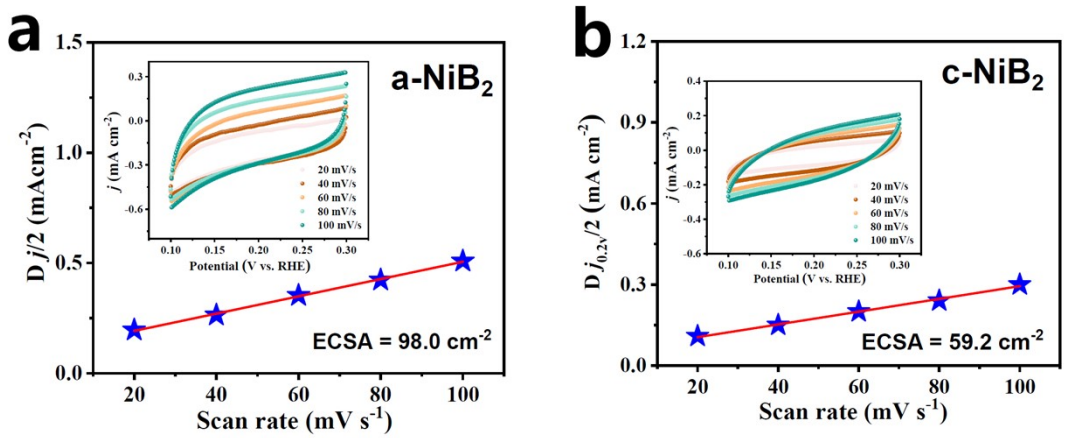

Fig. S9. CV measurements for determining the ECSA of (a) a-NiB_2 and (b) c-NiB_2.

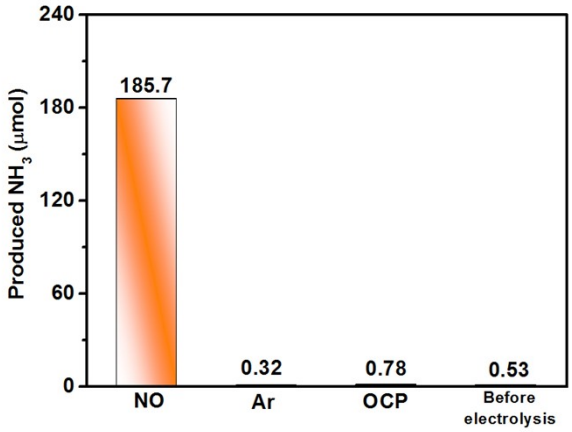

Fig. S10. Amounts of produced NH_3 on NiB_2 under different conditions at -0.4 V.

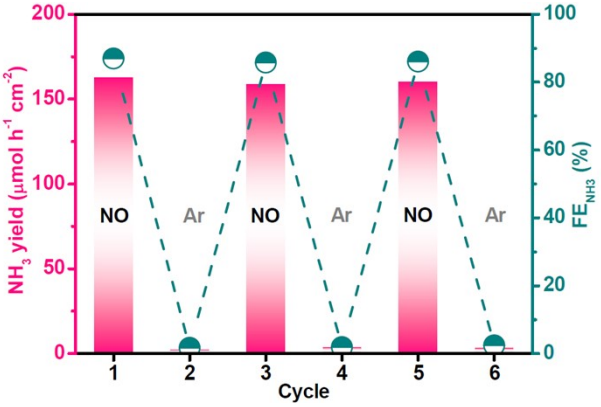

Fig. S11. Switching Ar/NO cycling tests on NiB_2 at -0.4 V.

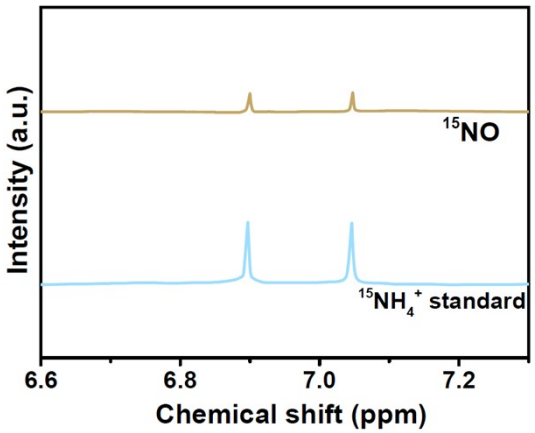

Fig. S12. ^{1}H NMR spectra of $^{15}NH_4^+$ standard sample and those fed by ^{15}NO and Ar after NORR electrolysis on NiB_2 at -0.4 V.

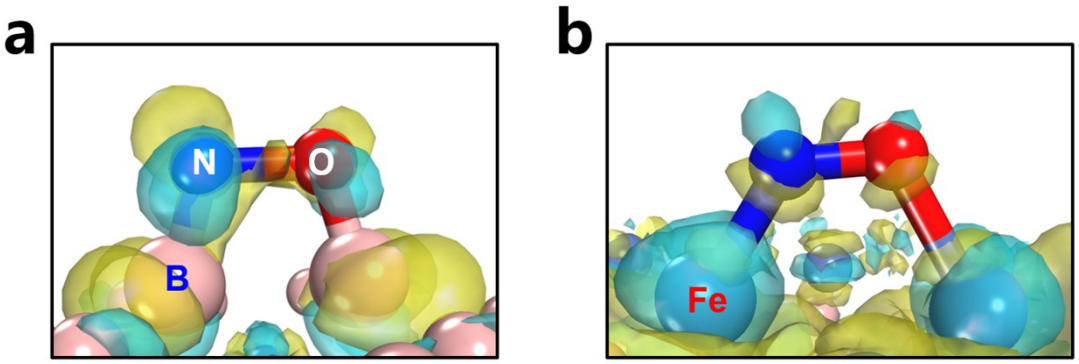

Fig. S13. Charge density differences of absorbed NO on (a) B and (b) Ni sites of NiB_2 (Yellow: accumulation, cyan: depletion).

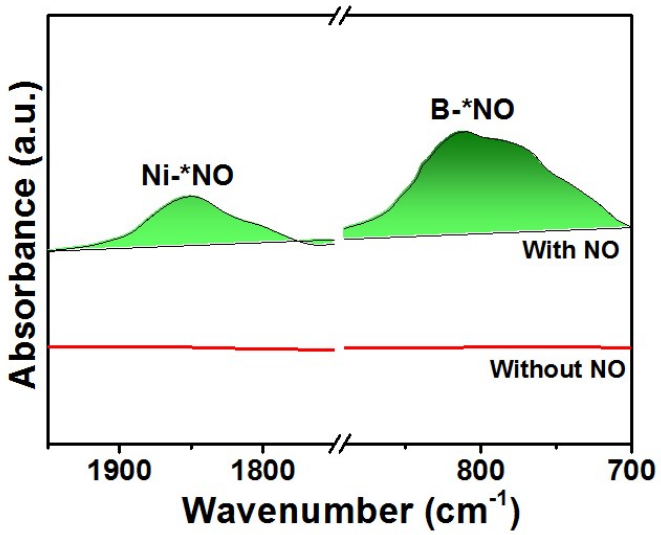

Fig. S14. FTIR spectra of NiB_2 with and without NO adsorption.

We perform FTIR measurement to experimentally investigate the NO adsorption behavior of NiB_2. It is seen that upon the adsorption of NO, the FTIR spectra show two distinct infrared peaks, where ~1850 cm^{-1} is assigned to NO adsorption on Ni species (Ni-*NO)[7], and ~800 cm^{-1} corresponds to B-*NO[8]. Obviously, the B-*NO peak area is much larger than Ni-*NO area, suggesting the stronger NO adsorption on B sites of NiB_2.

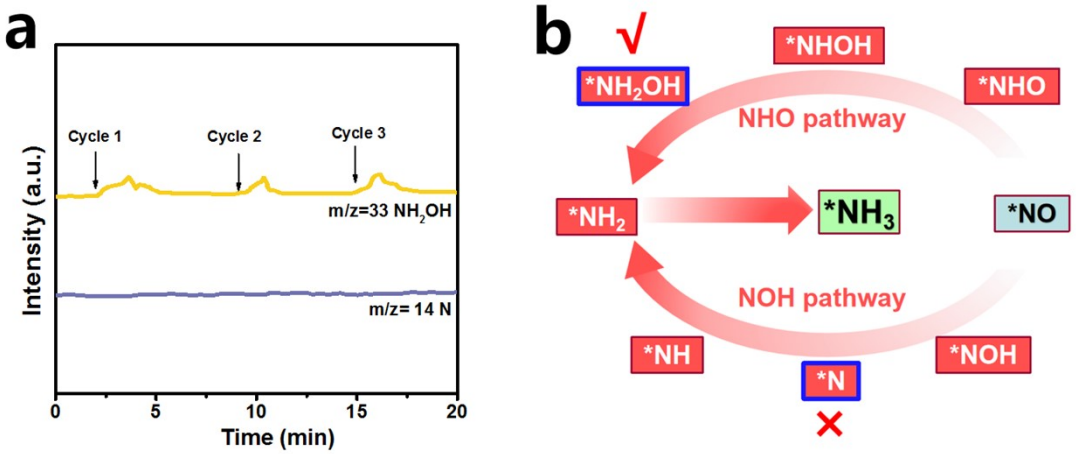

Fig. S15. (a) Online DEMS spectra of NiB_2 during the NORR electrolysis. (b) Schematic of two typical NORR pathways.

The online DEMS data (Fig. S15a) reveal an obvious sign of NH_2OH intermediate (m/z=33) but no detection of N intermediate (m/z=14), implying that NiB_2 prefers to adopt a NHO pathway (*NO → *NHO → *NHOH → *NH_2OH→ *NH_2 → *NH_3) rather than NOH pathway (*NO → *NOH → *N → *NH→ *NH_2 → *NH_3) to drive the NORR process[9], as illustrated in Fig. S15b.

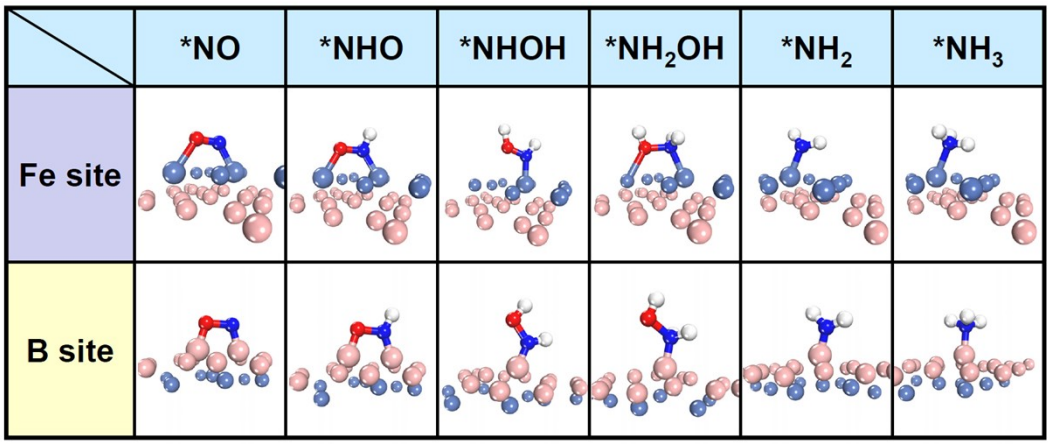

Fig. S16. Optimized structures of NORR intermediates on B and Ni sites of NiB_2.

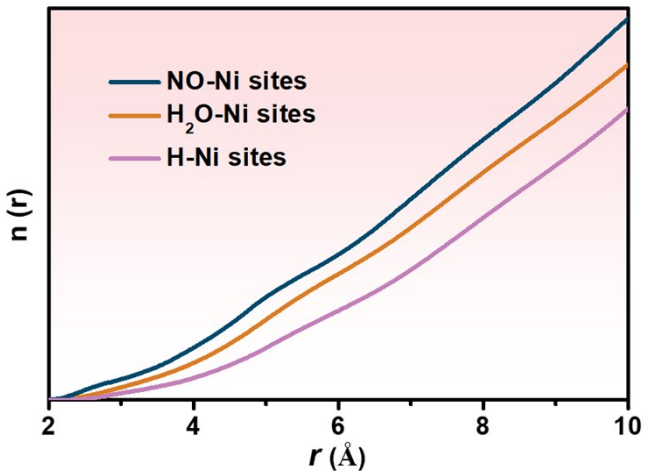

Fig. S17. Integrated RDF curves of *NO, *H_2O, and *H on Ni sites of NiB_2.

Table S1. Comparison of the optimum NH_3 yield and NH_3-Faradic efficiency (FE_{NH3}) for recently reported state-of-the-art NORR electrocatalysts at ambient conditions.

Catalyst	Electrolyte	NH_3 yield rate ($\mu mol\ h^{-1}\ cm^{-2}$)	FE_{NH3} (%)	Potential (V vs. RHE)	Ref.
Mo_2C	0.5 M Na_2SO_4	122.7	86.3	-0.4	[10]
Ni_2P/CP	0.1 M HCl	33.47	76.9	-0.2	[11]
$Ru_{0.05}Cu_{0.95}$	0.05 M Na_2SO_4	17.68	64.9	-0.5	[12]
Co_1/MoS_2	0.5M Na_2SO_4	217.6	87.7	-0.5	[9]
MoS_2/GF	0.1 M HCl	99.6	76.6	0.1	[13]
NiO/TM	0.1 M Na_2SO_4	125.3	90	-0.6	[14]
a-$B_{2.6}C@TiO_2$/Ti	0.1 M Na_2SO_4	216.4	87.6	-0.9	[15]
FeP/CC	0.2 M PBS	85.62	88.49	-0.2	[16]
Bi NDs	0.1 M Na_2SO_4	70.2	89.2	-0.5	[17]
CoP/TM	0.2 M Na_2SO_4	47.22	88.3	-0.2	[18]
CoS_{1-x}	0.2 M Na_2SO_4	44.67	53.62	-0.4	[19]
HCNF	0.2 M Na_2SO_4	22.35	88.33	-0.6	[20]
$Cu_2O@CoMN_2O_4$	0.1 M Na_2SO_4	94.18	75.05	-0.9	[21]
MoC/NCS	0.1 M HCl	79.4	89	-0.8	[22]
NiB_2	**0.5 M Na_2SO_4**	**167.1**	**89.6**	**-0.4**	**This work**

Supplementary references

[1]. J. Wu, M. Hou, Z. Chen, W. Hao, X. Pan, H. Yang, W. Cen, Y. Liu, H. Huang, P. W. Menezes and Z. Kang, *Adv. Mater.*, 2022, **34**, 2202995.

[2]. L. Zhang, J. Liang, Y. Wang, T. Mou, Y. Lin, L. Yue, T. Li, Q. Liu, Y. Luo, N. Li, B. Tang, Y. Liu, S. Gao, A. A. Alshehri, X. Guo, D. Ma and X. Sun, *Angew. Chem. Int. Edit.*, 2021, **60**, 25263-25268.

[3]. P. Li, Z. Jin, Z. Fang and G. Yu, *Energy Environ. Sci.*, 2021, **14**, 3522-3531.

[4]. X. Li, G. Zhang, P. Shen, X. Zhao and K. Chu, *Inorg. Chem. Front.*, 2023, **10**, 280-287.

[5]. B. He, P. Lv, D. Wu, X. Li, R. Zhu, K. Chu, D. Ma and Y. Jia, *J. Mater. Chem. A*, 2022, **10**, 18690-18700.

[6]. K. Chu, Y. Luo, P. Shen, X. Li, Q. Li and Y. Guo, *Adv. Energy. Mater.*, 2022, **12**, 2103022.

[7]. M. Mihaylov and K. Hadjiivanov, *Langmuir*, 2002, **18**, 4376-4383.

[8]. L. Li, C. Tang, X. Cui, Y. Zheng, X. Wang, H. Xu, S. Zhang, T. Shao, K. Davey and S. Z. Qiao, *Angew. Chem. Int. Edit.*, 2021, **133**, 14250-14256.

[9]. X. Li, K. Chen, X. Lu, D. Ma and K. Chu, *Chem. Eng. J.*, 2023, **454**, 140333.

[10]. K. Chen, P. Shen, N. Zhang, D. Ma and K. Chu, *Inorg. Chem.*, 2023, DOI: 10.1021/acs.inorgchem.2c03714.

[11]. T. Mou, J. Liang, Z. Ma, L. Zhang, Y. Lin, T. Li, Q. Liu, Y. Luo, Y. Liu, S. Gao, H. Zhao, A. M. Asiri, D. Ma and X. Sun, *J. Mater. Chem. A*, 2021, **9**, 24268-24275.

[12]. J. Shi, C. Wang, R. Yang, F. Chen, N. Meng, Y. Yu and B. Zhang, *Sci. China Chem.*, 2021, **64**, 1493-1497.

[13]. L. Zhang, J. Liang, Y. Wang, T. Mou, Y. Lin, L. Yue, T. Li, Q. Liu, Y. Luo, N. Li, B. Tang, Y. Liu, S. Gao, A. A. Alshehri, X. Guo, D. Ma and X. Sun, *Angew. Chem. Int. Ed.*, 2021, **133**, 25467-25472.

[14]. P. Liu, J. Liang, J. Wang, L. Zhang, J. Li, L. Yue, Y. Ren, T. Li, Y. Luo, N. Li, B. Tang, Q. Liu, A. M. Asiri, Q. Kong and X. Sun, *Chem. Commun.*, 2021, **57**, 13562-13565.

[15]. J. Liang, P. Liu, Q. Li, T. Li, L. Yue, Y. Luo, Q. Liu, N. Li, B. Tang, A. A. Alshehri, I. Shakir, P. O. Agboola, C. Sun and X. Sun, *Angew. Chem. Int. Ed.*, 2022, **61**, e202202087.

[16]. J. Liang, Q. Zhou, T. Mou, H. Chen, L. Yue, Y. Luo, Q. Liu, M. S. Hamdy, A. A. Alshehri, F. Gong and X. Sun, *Nano Res.*, 2022, **15**, 4008-4013.

[17]. Y. Lin, J. Liang, H. Li, L. Zhang, T. Mou, T. Li, L. Yue, Y. Ji, Q. Liu, Y. Luo, N. Li, B. Tang, Q. Wu, M. S. Hamdy, D. Ma and X. Sun, *Mater. Today Phys.*, 2022, **22**.

[18]. J. Liang, W.-F. Hu, B. Song, T. Mou, L. Zhang, Y. Luo, Q. Liu, A. A. Alshehri, M. S. Hamdy, L.-M. Yang and X. Sun, *Inorg. Chem. Front.*, 2022, **9**, 1366-1372.

[19]. L. Zhang, Q. Zhou, J. Liang, L. Yue, T. Li, Y. Luo, Q. Liu, N. Li, B. Tang, F. Gong, X. Guo and X. Sun, *Inorg. Chem.*, 2022, **61**, 8096-8102.

[20]. L. Ouyang, Q. Zhou, J. Liang, L. Zhang, L. Yue, Z. Li, J. Li, Y. Luo, Q. Liu, N. Li, B. Tang, A. Ali Alshehri, F. Gong and X. Sun, *J. Colloid Interf. Sci.*, 2022, **616**, 261-267.

[21]. C. Bai, S. Fan, X. Li, Z. Niu, J. Wang, Z. Liu and D. Zhang, *Adv. Funct. Mater.*, 2022, **32**, 2205569.

[22]. G. Meng, M. Jin, T. Wei, Q. Liu, S. Zhang, X. Peng, J. Luo and X. Liu, *Nano Res.*, 2022, **15**, 8890-8896.